Stacking order and Coulomb correlation effect in the layered charge density wave phase of $1T$-NbS_2

Wei Wang,[1,2] Chen Si,[2] Wen Lei,[3] Feng Xiao,[1] Yunhui Liu,[1] Carmine Autieri,[4] and Xing Ming[1,5,*]

[1]*College of Science, Guilin University of Technology, Guilin 541004, People's Republic of China*

[2]*School of Materials Science and Engineering, Beihang University, Beijing 100191, People's Republic of China*

[3]*Key Laboratory of Artificial Micro- and Nano-Structures of Ministry of Education and School of Physics and Technology, Wuhan University, Wuhan 430072, People's Republic of China*

[4]*International Research Centre MagTop, Institute of Physics, Polish Academy of Sciences, Aleja Lotników 32/46, PL-02668 Warsaw, Poland*

[5]*MOE Key Laboratory of New Processing Technology for Nonferrous Metal and Materials, Guangxi Key Laboratory of Optic and Electronic Materials and Devices, Guilin University of Technology, Guilin 541004, People's Republic of China*

(Received 16 September 2021; revised 29 November 2021; accepted 20 December 2021; published 11 January 2022)

Two-dimensional (2D) layered materials have attracted tremendous interest from the perspective of basic physics and technological applications in the last decade. Especially, the artificially assembled van der Waals (vdW) heterostructures and twisted 2D materials bring out fascinating properties, and render promising applications possible by engineering the stacking order. Here, based on first-principles calculations, we explored the interplay between stacking effect and electron-electron correlation effects in the layered vdW material of bulk $1T$-NbS_2 with a 2D charge density wave (CDW) order. Without considering the Coulomb correlation effects, two energetically favorable out-of-plane stacking configurations are identified: one is a metallic phase with a single-layer stacking pattern, another is a band insulator with a paired-bilayer stacking configuration. Even if the Coulomb correlation effects are taken into account, the two energetic favorable stacking orders are still far more stable than other stacking orders. Furthermore, increasing the Coulomb interactions, the paired-bilayer stacking configuration transforms from nonmagnetic band insulator to antiferromagnetic insulator, while the single-layer stacked $1T$-NbS_2 undergoes a Slater-Mott metal-insulator transition, which indicates the non-negligible role of electron-electron correlation interactions. In addition, the electronic structure and magnetic ground state change drastically among different stacking configurations, providing a platform to tune the electronic structures and interlayer magnetic interactions. In contrast to the widely accepted scenario of Mott localization as the driving force behind the gap formation in the CDW phase of layered transition-metal dichalcogenides, our results not only highlight the crucial role of stacking order in the electronic structures of $1T$-NbS_2, but also shed fresh light on the distinct effects of Coulomb interactions on different stacking arrangements.

DOI: 10.1103/PhysRevB.105.035119

I. INTRODUCTION

Two-dimensional (2D) layered materials exhibit diverse properties owing to the delicate interaction between the layers held together by weak van der Waals (vdW) forces, which attract considerable attention as potential materials for promising applications [1–3]. Furthermore, abundant physical properties of the vdW layered materials can be modulated by the interlayer interactions through intercalation, pressure, strain, twist, or stacking order. For example, the rotational degrees of freedom between layers can be controlled over to create new phenomena in known materials. Manipulating the twist angle between two 2D monolayers in vdW bilayer heterostructures can tune the band structures and electrical properties and realize twistronics devices [4,5]. In particular, the discovery of unconventional superconductivity, correlated insulating behavior, ferromagnetism, and topological phase in the magic-angle twisted bilayer graphene have sparked researchers' unprecedented enthusiasm [6–11].

On the other hand, lateral translation or sliding of one layer relative to another layer can modify the stacking order and stacking symmetry of the vdW layered materials, which gives rise to rich phase diagrams and novel properties, such as the stacking-engineered ferroelectricity in bilayer BN [12,13], stacking-tunable magnetism in bilayer CrI_3 and $CrBr_3$ [14,15], and stacking-driven metal-insulator transitions in layered $1T$-TaS_2 [16–19]. $1T$-TaS_2 is an archetypal charge density wave (CDW) material that has been in the spotlight for many years, which transforms into a commensurate CDW (CCDW) phase characterized by $\sqrt{13} \times \sqrt{13}$ star-of-David (SD) clusters (schematically shown in Fig. 1) upon cooling to ∼200 K [20]. Recently rekindled interest in $1T$-TaS_2 stems from the extensive debate on the origin of the insulating nature in the CCDW phase. According to traditional wisdom, there is one unpaired electron forming a half-filled band in the CCDW phase; therefore, the insulating ground state is driven by the Mott-Hubbard mechanism [21]. However, first-principles density-functional theory

*mingxing@glut.edu.cn

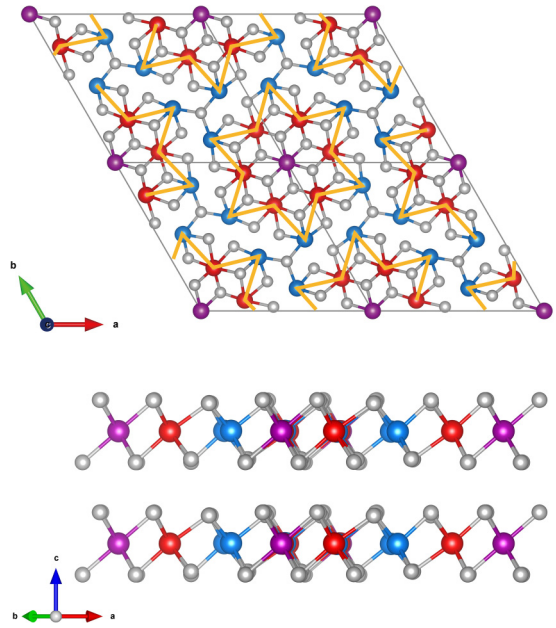

FIG. 1. Top and side views of the CCDW phase of $1T$ polytype TaS_2 or NbS_2 characterized by the $\sqrt{13} \times \sqrt{13}$ SD clusters (schematically drawn in yellow line). The big balls denote the Ta or Nb atoms (the purple, red, and blue colors indicate three atomic sites with different structural symmetry), and the small balls (gray color) represent the S atoms.

(DFT) calculations combined with transport measurements, angle-resolved photoemission spectroscopy (ARPES), low-energy electron diffraction experiments, and atomic resolution scanning transmission electron microscopy (STEM) give robust evidence that the insulating gap of the CCDW phase is primarily governed by the out-of-plane stacking arrangements of the SD clusters rather than the electron-electron correlation [16–19,22–30]. These theoretical and experimental results highlight the critical role played by the stacking order of the SD clusters intertwining with orbital order in determining the electronic structure of the CCDW phase.

Recently, we and Tresca *et al.* theoretically predicted that $1T$-NbS_2 belongs to CDW materials, which is isostructural and isovalent to $1T$-TaS_2 and also exhibits the typical $\sqrt{13} \times \sqrt{13}$ SD structural reconstructions (Fig. 1) [31,32]. In the bulk-phase NbS_2, the unit cell of $1T$ polytype consists of monolayer NbS_2 with corner-sharing NbS_6 octahedra, which differs from the $2H$ and $3R$ polytypes with bilayer and trilayer stacking arrangements of the corner-sharing trigonal prismatic coordination NbS_6 layers [33–35]. The distinct stacking arrangements of the coordination polyhedra lead to dramatically different electronic structures ranging from insulator to metal to superconductor for these three polytypes of layered NbS_2 [31–38]. The monolayer $1T$-NbS_2 exhibits a ferromagnetic (FM) spin-1/2 insulating state [32], while an interlayer antiferromagnetic (AFM) ordering may dominate the interlayer coupling in the bulk phase [31]. Diffuse x-ray scattering measurements detect traces of CDW in $2H$-NbS_2, which is also attributed to the local $1T$ polytype environment at the interface of the rotational stacking faults between $2H$ domains [35]. Martino *et al.* propose that the magnetic CDW state of the $1T$-NbS_2 layers can intercalate the host of $2H$ stacking NbS_2 and form a $2H/1T$-NbS_2 heterostructure, resulting in an unexpected unidirectional Kondo scattering in metallic $2H$-NbS_2 [38]. The stacking order is expected to create lateral shifts of the CDW clusters between adjacent layers and provide an effective route to manipulate the electronic phases of the layered $1T$-NbS_2. Furthermore, being the same as the CCDW phase of $1T$-TaS_2, the unit cell of $1T$-NbS_2 is reconstructed into a triangular lattice with prototypical SD clusters, and there is a single unpaired electron with $S = 1/2$ spin moment localizing in the centers of each SD cluster [31,32]. Therefore, exotic quantum phases such as quantum spin liquid are expected to emerge in these triangular-lattice materials [39–45].

The motivation of the present paper is to further examine the out-of-plane stacking order of the SD clusters in the CCDW phase by first-principles DFT calculations, and uncover the role played by the stacking order and electron-electron correlation in the stability and electronic phase of $1T$-NbS_2. We not only unveil the tunable electronic structures derived from the distinct stacking order of the SD clusters, but also reveal a significant effect of the Coulomb correlation in manipulating the electronic properties of the CCDW phase $1T$-NbS_2. We hope our theoretical results will stimulate further experimental and theoretical studies on the electronic properties of the CCDW phase to better understand the intricate interplay between the stacking order and electron correlation in $1T$-NbS_2. Furthermore, although we examine the case of the $1T$-NbS_2, similar effects could be present in other members of the same material class.

II. STRUCTURE MODELS AND COMPUTATIONAL DETAILS

The routinely stacked CCDW phase of $1T$-NbS_2 can be described by the space group of $P\bar{3}$. Each Nb atom is bonded to six S atoms forming distorted octahedral coordination, and the adjacent layers are bonded together by weak vdW forces (the schematic model is presented in Fig. 1). The building block of the CCDW phase is the SD cluster as shown in Fig. 2(a). Due to the threefold in-plane rotational symmetry of the CCDW phase, five kinds of Nb atoms can be defined, where the central Nb atom is labeled as 0 and the surrounding Nb atoms are labeled as 1 to 4 in each SD cluster, respectively. Taking the threefold in-plane symmetry into account, the out-of-plane alignments of the SD clusters in adjacent planes are described by five types of stacking interfaces t_i ($i = 0, 1, 2, 3, 4$) [illustrated in Figs. 2(b)–2(f)], which lead to five types of out-of-plane three-dimensional stacking order T_i ($i = 0, 1, 2, 3, 4$). The routinely stacking configuration T_0 consists of on-top stacked monolayer with the stacking interface t_0 [Fig. 2(b)], whereas other single-layer stacking configuration T_i can be viewed as a lateral shift [the dashed line depicted in Figs. 2(c)–2(f)] of every single layer with respect to the adjacent layer with the corresponding stacking interface t_i. Accordingly, the central Nb atoms of the SD in the upper layer are located above the Nb atoms in one of the tips (t_1 and t_4 interfaces) or the inner circle hexagon (t_2 and t_3 interfaces) of the SD of the lower layer. In addition, we also considered paired-bilayer stacking configurations with

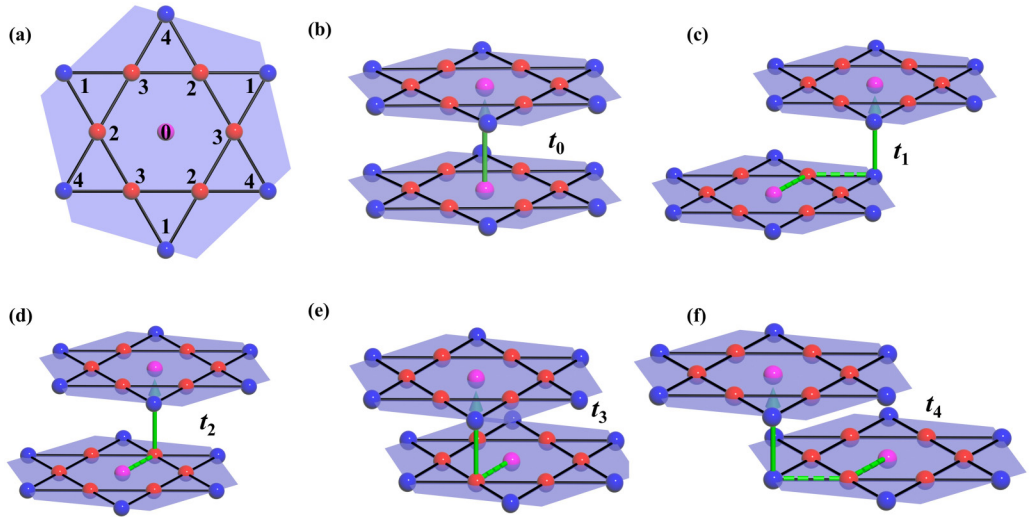

FIG. 2. Schematic illustration of the $\sqrt{13} \times \sqrt{13}$ SD cluster in the CCDW phase of $1T$ polytype NbS_2 and different out-of-plane stacking orders (the S atoms are not shown). (a) In-plane SD cluster and classification of the Nb atoms. (b)–(f) are five kinds of stacking interfaces (t_0–t_4) between two adjacent layers. Solid green arrows illustrate the Nb atom in the first layer facing the central Nb atom in the adjacent layer, and dashed green lines denote the in-plane lateral shift of the SD clusters with respect to the counterparts in the adjacent layer.

a lateral sliding of every two layers due to the possibility of the Peierls dimerization for a chain of half-filled bands. These four types of stacking order T_{0i} ($i = 1, 2, 3, 4$) can be viewed as on-top stacked bilayers with the stacking interface t_0, which by themselves are stacked by a stacking interface t_i ($i = 1, 2, 3, 4$) in the out-of-plane direction [16,17,22,27]. All these stacking orders are illustrated in detail in Fig. 3.

Based on DFT, we performed all of the calculations by using the Vienna *Ab initio* Simulation Package (VASP) [46,47] within the generalized gradient approximation (GGA) [48] approach and projector-augmented wave [49] potentials. The kinetic-energy cutoff of 520 eV was used, and Brillouin zone was segmented by Gamma centered grid of $0.2\,\text{Å}^{-1}$ for all structures [50]. During the structural optimization and band-structures calculation stages, the Gaussian smearing method is used with a small smearing width of 0.02 eV, and tetrahedron method with Blöchl corrections is used for self-consistent and density-of-state calculations to obtain accurate energy. The conjugate gradient algorithm was used to perform the structural energy minimization, and the convergence criteria were set to 10^{-6} eV and 0.01 eV/Å for total energy and atomic force, respectively. Considering the weak interlayer interactions in the CCDW phase, zero damping DFT-D3 method of Grimme vdW dispersion correction [51] was employed

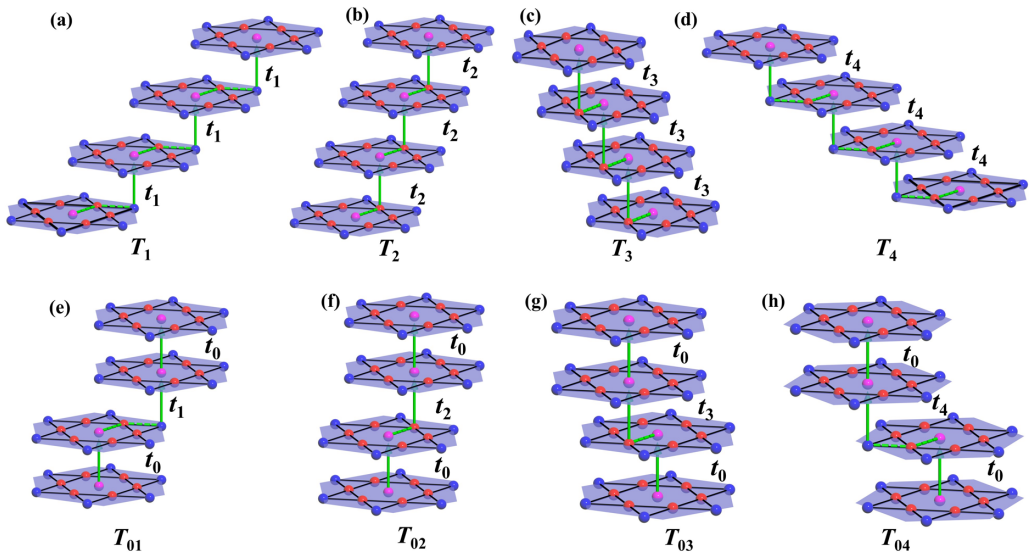

FIG. 3. Schematics of the out-of-plane stacking orders (the S atoms are not shown) of the SD clusters in the CCDW phase of $1T$-NbS_2: (a)–(d) are four kinds of stacking patterns of T_1–T_4 with corresponding interlayer interface t_i (t_1–t_4) between two adjacent layers; (e)–(h) are four kinds of bilayer stacking patterns of T_{01}–T_{04} with corresponding interlayer interface t_i (t_1–t_4) between two adjacent on-top stacked bilayers with t_0 interface.

TABLE I. Equilibrium layer spacing (c) and energy landscape of the different stacking configurations for the NM states calculated within GGA. The changes of the layer spacing (Δc), total energy ($\Delta E_{\rm tot}$), vdW energy ($\Delta E_{\rm vdW}$), and formation energy ($\Delta E_{\rm f}$) are calculated with respect to the T_0 stacking order.

Stacking order	c (Å)	Δc (%)	$\Delta E_{\rm tot}$ (meV/SD)	$\Delta E_{\rm vdW}$ (meV/SD)	$\Delta E_{\rm f}$ (meV/SD)
T_0	5.926	0	0	0	0
T_1	5.887	−0.658	−24.82	−75.77	−23.16
T_2	5.910	−0.270	6.45	−29.72	2.46
T_3	5.909	−0.287	12.11	−31.28	8.89
T_4	5.900	−0.439	27.59	−46.79	24.32
T_{01}	5.908	−0.304	−36.29	−36.54	−43.08
T_{02}	5.920	−0.101	−4.57	−11.58	−12.96
T_{03}	5.920	−0.101	0.21	−10.96	−8.69
T_{04}	5.923	−0.051	−5.51	−4.87	−12.53

to perform geometrical optimization, so that accurate lattice information and total energy can be obtained. We also carried out structural optimization and calculated the total energy within another vdW correction method of optB88-vdW functionals [52,53]. As shown in Table S1 in the Supplemental Material (SM) [54], although the equilibrium layer spacing predicated by the optB88-vdW functionals has some variations, the calculated energy differences by the two vdW methods are very similar. The relative stability of the stacking order remains unchanged; therefore, we just presented the results calculated with vdW dispersion correction of DFT-D3 in the main text. To deal with the electronic correlation, we add the Coulomb repulsion U on the 4d orbitals of the Nb ranging from 0 to 3.5 eV, which are typical values for 4d orbitals. In order to evaluate the stability of the stacking patterns, we defined the average interlayer formation energy according to the equation $E_f = \frac{E_{\rm bulk} - \sum_{i=1}^{N} E_i}{N}$, where $E_{\rm bulk}$ is the total energy of a certain stacking pattern, $E_{\rm i}$ is the energy of the corresponding isolated monolayer of the bulk, and N is associated with the number of layers in the stacking system.

III. RESULTS AND DISCUSSION

Firstly, the normal on-top vertically stacking order T_0 of the CCDW phase [Fig. 2(b)] serves as the starting point of our study. The optimized lattice parameters are $a = 12.129$ Å and $c = 5.926$ Å at the DFT-D3 level, which are consistent with previous results [31]. In agreement with our previous results [31], without considering electronic correlations the CCDW phase always converges to a nonmagnetic (NM) metallic state independent of the preset magnetic configuration. When we add the Coulomb interaction, the magnetic ground state is an interlayer AFM state that simultaneously opens a band gap (Fig. S1 in the SM) [54]. However, as shown in Table I, the calculated results indicate that the stacking order plays an essential impact on the layer spacing and stability. The total energy of the system depends remarkably on the stacking order and varies up to ∼60 meV/SD. Compared with the T_0 stacking order, the layer spacing shrinks a bit and results in significant changes of the vdW energy, where the vdW energy $\Delta E_{\rm vdW}$ is positively proportional to the change of the layer spacing Δc. The vdW energy decreases as the layer spacing shrinks, demonstrating the crucial role of the vdW interactions is to anchor the layers [55]. The calculated results imply that there are no obvious correlations between total energy and the vdW interactions, whereas the average interlayer formation energy can describe the relationship better between the stacking orders and the total energy.

Furthermore, two stacking configurations of T_1 and T_{01} exhibit remarkable stability from an energetic viewpoint. T_1 stacking order is the most favorable stacking arrangement for the vdW energy. On the contrary, although the benefit of vdW energy is not significant, T_{01} stacking is preferred by total energy and formation energy. Both T_1 and T_{01} stacking orders are featured by the highly stable t_1 interface over the other interfaces, which are closely related to the favorable vdW interaction and interlayer S–S bonding [22]. In fact, the interlayer S atoms configurations in different stacking systems are distinct from each other upon the specific stacking order. Shorter or longer S–S distances can be observed in the layer spacing. Such a steric effect of the S atoms plays a significant impact on the energy of the stacking system. A shorter S–S distance results in an interlayer bonding with the $3p_z$ orbitals, which is favorable for energy, but such a bonding interaction is disallowed for a longer S–S distance. As exemplified by T_1 and T_4 stacking orders, we can clearly identify the different interlayer distances between the nearest-neighbor S atoms coordinated with the central Nb atoms of the SD cluster [Figs. 4(a) and 4(b)]. As shown in the corresponding charge density maps [Figs. 4(c) and 4(d)], bonding behavior can be clearly observed for the T_1 stacking with an interlayer S–S distance of ∼3.29 Å, whereas no such trace for the T_4 stacking with the interlayer S–S distance of ∼4.71 Å. Furthermore, as shown in Fig. S2 in the SM [54], no obvious bonding behavior has been observed between the S atoms of the T_2 and T_3 stacking order with t_2 and t_3 interfaces.

In addition, the nonmagnetic electronic structures show obvious dependence on the stacking arrangements of the CCDW phase (see Fig. 5 and Fig. S3 in the SM) [54]. In particular, the relative position of the SD clusters in adjacent ab planes has a significant influence on the band dispersions. All the $T_{\rm i}$ stacking patterns show metallic behavior; whereas partial $T_{0\rm i}$ stacking orders show semiconducting behavior and some show metallic behavior, the electronic structure and transport properties of the $T_{0\rm i}$ stacking arrangements show striking variations associated with the stacking orders. As shown in Fig. 5(a), the T_1 stacking is metallic with a half-filled band

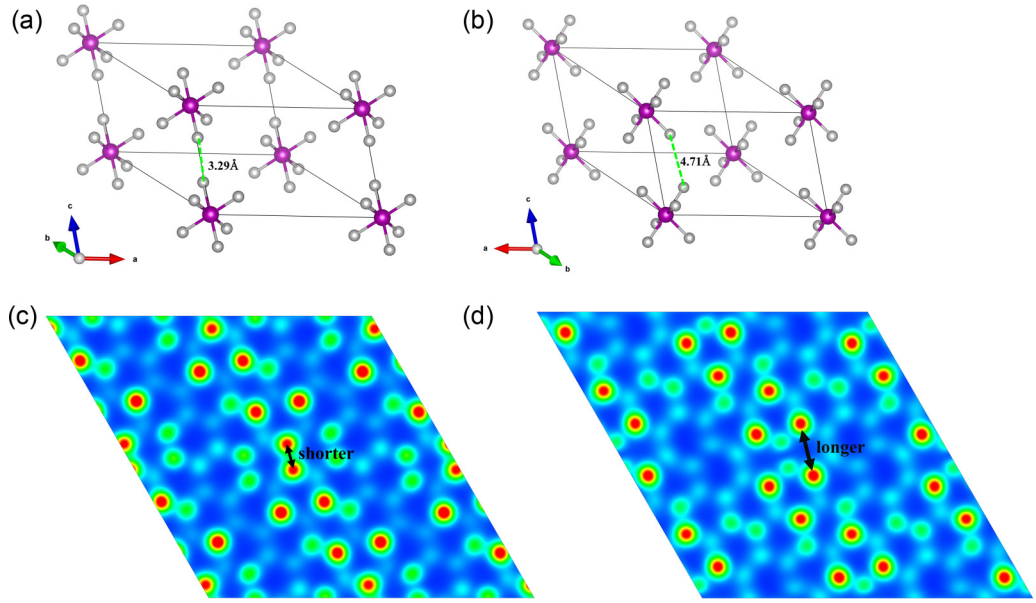

FIG. 4. (a), (b) Side views of the T_1 and T_4 stacking orders (only the central Nb atoms of the SD cluster and the coordinated S atoms are shown). (c), (d) Charge density maps corresponding to the T_1 and T_4 stacking orders, respectively, obtained by integrating electronic states near the Fermi level. The slices are located at the center of t_1 and t_4 interfaces and parallel to the *ab* plane.

characterized by the $4d_{3z^2-r^2}$ orbital contribution from the central Nb atom of the SD clusters. Due to the presence of the $4d_{3z^2-r^2}$ bands at the Fermi level, the electronic properties strongly depend on the stacking manner along the z axis. Attributed to the interlayer S–S bonding interactions [Fig. 4(a)], the T_1 stacking order shows a significant in-plane hopping [17] and stronger three-dimensional metallicity, where the bands cross the Fermi level not only along Γ–A but also along L–A and L–H. By contrast, the special orbital order intertwined with the CDW in the T_0 stacking only permits significant out-of-plane charge hopping, corresponding to the in-plane insulating characteristics along Γ–M–K and out-of-plane one-dimensional metallic band dispersion along Γ–A [31]. Furthermore, as shown in Fig. 5(b), an inherent band gap of 45.9 meV is opened up for the T_{01} stacking within the GGA approach, implying a band-insulating behavior instead of Mott insulator. Each cell is constructed from two SD clusters, and a pair of degenerate bands is almost completely isolated in the uppermost valence band. The contributions of the $4d_{3z^2-r^2}$ characteristics from the two central Nb-0_1 and Nb-0_2 atoms of the two SD are almost the same, indicating a degeneracy of them. A cell with an even number of electrons can yield filled valence bands forming an insulator or semiconductor [56]. Obviously, two orphan electrons from Nb-0_1 and Nb-0_2 pair with each other and fill the isolated orbit, accompanied by an opening of the band gap and a lowering of the total energy. Therefore, the stacking arrangements enable one to manipulate the band dispersion and gap structure of the CCDW phase 1T-NbS_2. Similar to 1T-TaS_2, the stacking order yields a device concept, which utilizes metastable stacking orders to control the electronic structure of nanostructures and causes a semiconductor-metal transition [17].

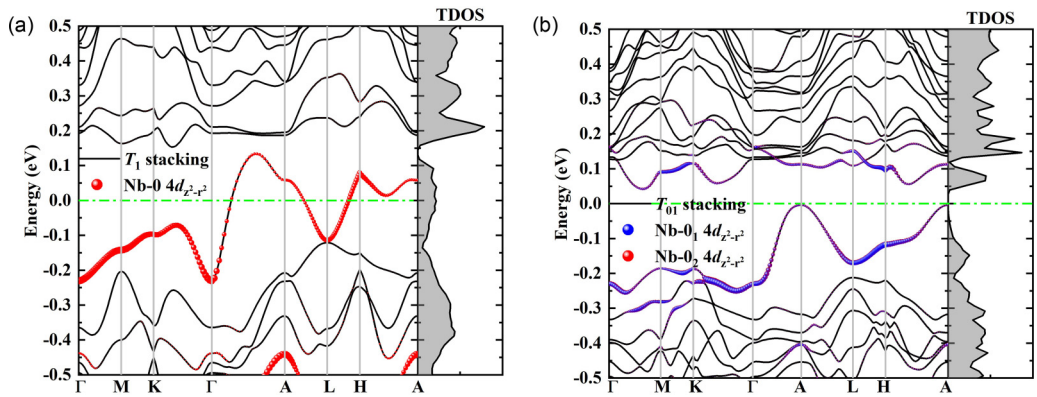

FIG. 5. Nonmagnetic band structures and corresponding total density of states (TDOS) of the (a) T_1 and (b) T_{01} stacking order within GGA approach. The red balls in (a) denote the orbital contributions with $4d_{3z^2-r^2}$ character of the central Nb atom of the SD cluster (Nb-0). The blue/red balls in (b) denote the orbital contributions with $4d_{3z^2-r^2}$ character of Nb-0_1/Nb-0_2 (central Nb atom of the SD in the first/second layer).

Attributed to the stacking effects, a band insulator is identified by interlayer dimerization in the T_{01} stacking of the CCDW phase $1T$-NbS_2, which is in contrast to the Mott-Hubbard mechanism proposed in previous studies on the origin of the insulating nature in the CCDW phase of $1T$-TaS_2 and monolayer $1T$-NbS_2 [24,32]. However, recent studies on $1T$-TaS_2 have also implied that this dimerization cannot be simply depicted by a genuine Peierls mechanism if the continuity of order parameter has been taken into account, which is strongly related to the interlayer hopping [16–18,22,23,25]. It is worth noting that the T_{01} stacking consists of two interfaces: the t_0 interface inside each on-top stacked paired bilayer and the t_1 interface between the adjacent bilayers. Once a stacking order is established, the interlayer hopping integral between adjacent layers will be changed dramatically, which has an essential impact on the electronic structure. The interlayer hopping in the t_0 interface is the same in the T_0 stacking, while interlayer hopping is much greater in the t_0 interface than the t_1 interface in the T_{01} stacking [18]. Moreover, there exists a continuous crossover region between the band-insulating phase and Mott-insulating phase in the bilayer Hubbard system, and the stronger interlayer hopping is beneficial to the band insulator [57,58]. Similar to previous findings for $1T$-TaS_2, the strong electron-electron correlation does not play a major role in the insulating nature of the T_{01} stacking, whereas the on-top stacked bilayer and the interlayer hopping should be the most important factors [16,22].

Even though the band-insulating behavior can be realized by paired SD layers without considering the electron-electron correlation [16,17,22], the strong correlations and Mott physics still exist in the limit of monolayers [32]. Furthermore, the orphan electron on each SD cluster provides $S = 1/2$ spin moment in the triangle lattice, which offers an opportunity to study the Coulomb correlation effects and quantum state in the CCDW phase of bulk $1T$-NbS_2. By considering Coulomb correlations at the level of $U = 2.95$ eV [31,59], we calculate the energy differences between different stacking configurations to explore the effects of the electron-electron correlation on the relative stability and the electronic structures. Especially, by doubling the cell along the out-of-plane stacking direction, two magnetic ordering states of AFM ↑↓ and FM↑↑ are preset for T_i stacking, whereas four magnetic states of AFM↑↓↑↓, AFM↑↓↓↑, AFM↑↑↓↓, and FM↑↑↑↑ are considered for T_{0i} stacking. As shown in Fig. 6, the magnetic ordering states exhibit lower energy relative to the NM state for all stacking patterns, which implies possible magnetic states at low temperature. The unpaired single-layer T_i stacking patterns, especially the T_1 and T_4 stacking arrangements, show stronger responses to the magnetic ordering and Coulomb correlation. By contrast, the energy gains of the T_{0i} stacking are not so striking, so that the energy of the AFM state and the NM state differs by only a few meV/SD. Moreover, the distinct stacking arrangements and interfaces show different magnetic configurations. For instance, the T_4 stacking tends to form FM↑↑ state rather than AFM↑↓ state, and T_{04} stacking tends to form AFM↑↓↓↑ state rather than AFM↑↓↑↓ state, implying that the t_4 interface is prone to form FM↑↑ configuration. In accord with the T_0 stacking, the t_0 interface tends to form AFM paired bilayers; all the T_{0i} stacking orders favor AFM↑↓ configurations in the t_0 interface. Therefore, a variation of the stacking orders by a lateral sliding could change the direct hopping strength between interlayer S orbitals, which further alters the interlayer magnetic interactions between FM and AFM ones. The stacking order provides an effective way to tailor the interlayer magnetic interactions, which opens a paradigm for seeking metamagnetic 2D materials from AFM to FM state in real applications [14,15].

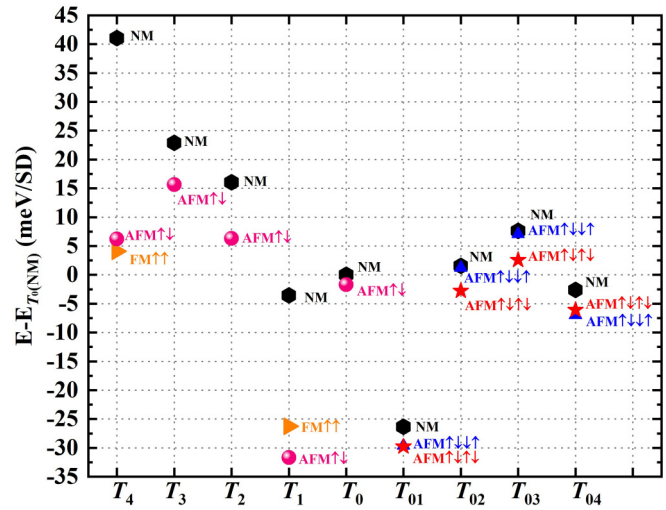

FIG. 6. Energy landscape of different stacking order with respect to T_0 stacking of the NM state. All magnetic ordering states are calculated by GGA + U within the Coulomb correlation of $U = 2.95$ eV. The upward and downward arrows represent the directions of the spin magnetic moments in different layers. We should note that not all our preset magnetic configurations are displayed here, because the unstable magnetic states have converged to NM state or other AFM states as depicted in the figure.

The T_1 and T_{01} stacking configurations are still far more stable than the other stacking orders (by ∼30 meV/SD) (Fig. 6). As shown in Fig. 7, the magnetic moments of the T_1 and T_{01} stacking orders in adjacent layers are antiparallel, confirming the interlayer AFM ordering. The magnetic moments are mainly concentrated in the central Nb atom of the SD clusters, while the other atoms only have negligible magnetic moments, which coincides well with the anticipation of lone electron with $S = 1/2$ spin moment localizing in the centers of each SD cluster. Surprisingly, the T_1 stacking obtains a huge energy gain after entering the magnetic ordering states, so that the total energy is lower than that of the T_{01} stacking by about 1.9 meV/SD. In addition, in contrast to the metallic band structure of the NM state, a tiny insulating gap of 12.9 meV is opened up for the AFM state (Fig. 8), which signifies the Slater-Mott insulating nature of the T_1 stacking (will be discussed in detail later). The electron-electron correlation and magnetic interactions play a minor impact on the T_{01} stacking; the energy differences between the NM and AFM states are within only 3 meV/SD. The two AFM states (AFM↑↓↓↑ and AFM↑↓↑↓) of the T_{01} stacking order almost have identical energies, indicating that the T_{01} stacking is not sensitive to the interlayer magnetic configurations, and the typical characteristics of the band insulator are robust. This phenomenon is consistent with the recent experimental confirmation that

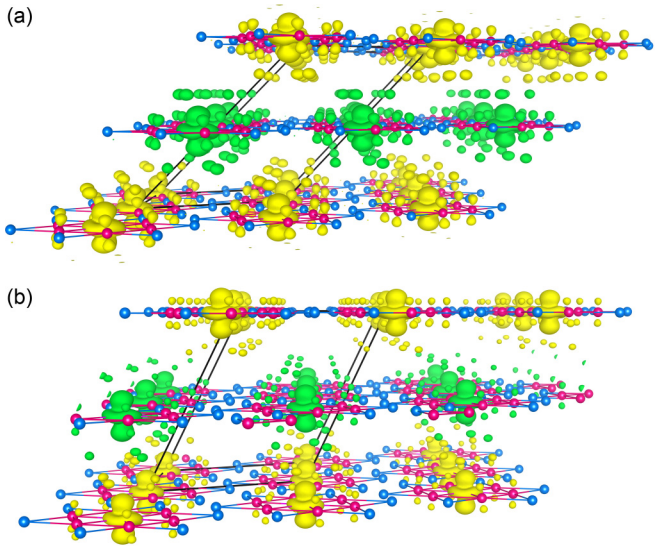

FIG. 7. The AFM spin density of the (a) T_1 and (b) T_{01} stacking orders. Spin-up (-down) isosurfaces are depicted in orange (green), which are displayed with an isosurface value of 0.0025 e/bohr^3.

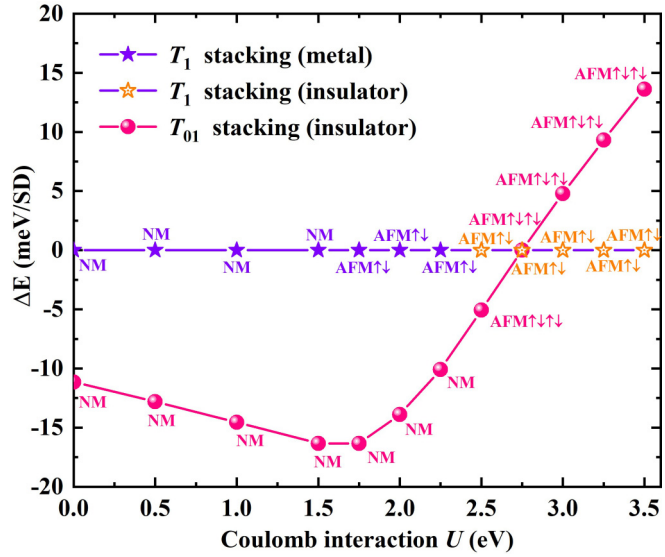

FIG. 9. The evolutions of the energy differences and metal-insulator transitions between T_1 and T_{01} stacking along with the increasing Coulomb correlation parameters U.

the paired bilayer T_{01} stacking is the dominant building block of $1T$-TaS_2 at low temperatures [18,25]. As stated above, the primary origin of the insulating properties in T_{01} stacking is the dimerization and interlayer hopping, while strong electron-electron correlation does not play a key role. In other words, T_{01} stacking is insensitive to Coulomb repulsion U, in contrast to the case of the T_1 stacking.

Compared with the T_{01} stacking order, the distinct insulating mechanisms lead to the compensation of the total energy for T_1 stacking under the action of U, which eventually results in a lower-energy stacking order. Notable is that the total energy difference between the T_1 and T_{01} stacking configurations is only ∼2 meV/SD. The CCDW phase of bulk $1T$-NbS_2 provides a platform to reveal the underlying role of U in the ground state with different stacking orders. Considering that the Nb element has a $4d$ shell with moderate

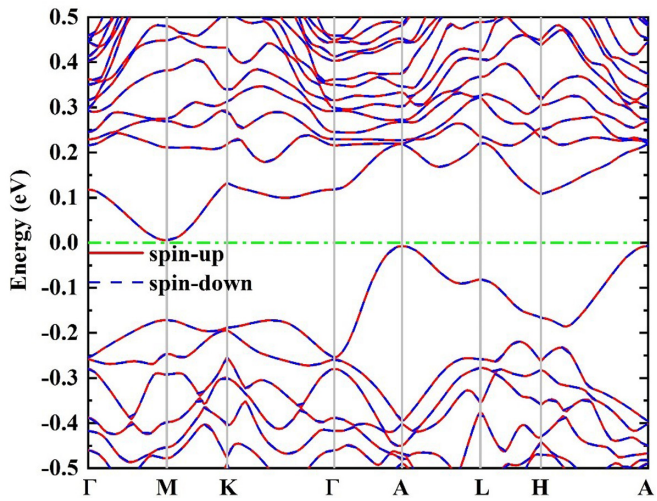

FIG. 8. Band structure of the interlayer AFM state for T_1 stacking calculated by GGA + U (U = 2.95 eV).

electron-electron correlation, we choose the U value ranging from 0 to 3.5 eV. As shown in Fig. 9, the T_{01} stacking order converges to NM insulating state when the U values are lower than 2.5 eV; then, the NM insulating state transforms to an AFM insulating state when the U value reaches up to 2.5 eV. Dynamical mean-field theory studies on the bilayer Hubbard model have identified a crossover from band insulator to Mott insulator under the effect of increasing U values [57,58]. On the contrary, the T_1 stacking order shows lower-energy NM metallic states when the U values are lower than 1.5 eV, and the energy differences between the T_1 and T_{01} stacking orders gradually increase with the increasing U value. Once the T_1 stacking order transforms from the NM metallic state to AFM metallic state at U = 1.75 eV, the evolution trend of the energy differences shows an upturn, which gradually decreases with the increasing U values. When the U value reaches up to 2.5 eV, the T_1 stacking order transforms from the AFM metallic state to an AFM insulating state. Therefore, both Coulomb repulsion and magnetic order are necessary to open the gap in the T_1 stacking order, which is a signature of a Slater-Mott insulator [60–62]. We can claim that along with the increasing U values, the T_1 stacking order exhibits an interesting Slater-Mott metal-insulator transition from NM metal to AFM metal and finally to AFM insulator. Along with the U value further increasing, the energy differences between the T_1 and T_{01} stacking orders gradually decrease. As a result, the ground state transforms from the band insulator to the Slater-Mott insulator. Previous calculations suggest that the band insulator may be so fragile that electronic doping or applying strain can easily destroy the relative stability of the two stacking configurations [22]. We speculate that the CCDW phase of bulk $1T$-NbS_2 is located at the crossover region of Slater-Mott insulator and band insulator, remaining to be uncovered experimentally. More precisely, both Coulomb repulsion and magnetism are needed to open the band gap making these states a Slater-Mott insulator.

The bilayer-stacked bulk phase of $1T$-NbS_2 and $1T$-TaS_2 may satisfy the criteria of a simple band insulator, but ARPES and x-ray diffraction data have suggested certain randomness of the out-of-plane stacking order, and STEM topographic images show the broken dimerization by unpaired SD clusters at the surfaces of the CCDW phase $1T$-TaS_2 [18,25]. These experiments demonstrate the possible existence of an unpaired stacking SD cluster accompanied with a small change of stacking order, which will yield band insulator to Mott insulator transitions and metal-insulator transitions. The small energy differences between the T_1 and T_{01} stacking order together with the possible stacking faults and stacking disorder in real materials will give rise to complex phase diagrams for the CCDW phase of $1T$-NbS_2. Additionally, the electron-electron correlation cannot be absolutely precluded, Mott physics might still play an important role in the electronic structure of the CCDW phase [16]. We note that first-principles calculations within traditional DFT, DFT+U, and the hybrid functional have failed to reproduce the out-of-plane insulating behavior of the bulk $1T$-TaS_2 for the T_0 stacking order with on-top stacked SD clusters [16,17,22,26,63]. Recently, a Mott-insulating band structure with the interlayer AFM order has been successfully achieved by applying the U potential onto a generalized basis [64]. However, no magnetic ordering has been observed in $1T$-TaS_2 so far [41–45]. In contrast, the calculated electronic structures show a band-insulating behavior without considering the magnetic configurations in the CCDW phase of $1T$-NbS_2, which transforms to Slater-Mott insulating state by considering the magnetic ordering states and Coulomb correction with DFT + U. Experimentally, it is difficult to synthesize the bulk-phase $1T$-NbS_2; only few-layer thin film and monolayer have been reported [35,65]. Recently, Martino *et al.* observed a signature of the Kondo effect in $2H$-NbS_2, a scattering of conduction electrons of dilute localized magnetic moments [38]. They argued that the magnetic moments originate from layers of $1T$-NbS_2, undergoing a CDW reconstruction with each superlattice cell hosting a lone spin, cause a Kondo effect observable only when the current flows across these planes. We think this experimental work provide evidence to support the magnetism in this material. Furthermore, the energy differences of the magnetic ordering states between the most stable T_1 and T_{01} stacking order are very small, which implies a possible magnetic disordering associated with the triangular lattice. The stacking-driven metal-insulator transitions in $1T$-NbS_2 are similar to thickness-driven metal-insulator transitions in transition-metal oxides, where in both cases the structural effects are responsible for a bandwidth reduction and consequently for a thickness-controlled metal-insulator transition towards more correlated electronic phases [60–62]. The presence of different electronic and magnetic phases paves the way to manipulate the competition between these phases by doping or applied external pressure. The concomitant insulating nature, localized orphan spin, and possible magnetic disordering on the triangular lattice of CCDW phase $1T$-NbS_2 will induce exotic quantum states, perhaps the elusive quantum spin liquid, needing to be further clarified both theoretically and experimentally.

IV. CONCLUSIONS

In summary, we explored the influences of stacking order and electron correlation effects on the electronic properties of the CCDW phase $1T$-NbS_2 by first-principles calculations. The electronic structures show a significant dependence on the stacking order. Without considering the electron-electron correlation, two energetically favorable stacking orders of T_1 and T_{01} show distinct electronic structures: one is metal and the other one is band insulator. These two energetically favorable stacking orders are still robust while considering the electron-electron correlation. Particularly, the ground state of the system is strongly related to the strength of the electron-electron correlation. Along with the increasing Coulomb interactions, the T_1 stacking order undergoes a Slater-Mott metal-insulator transition, whereas the T_{01} stacking order transforms from band insulator to AFM insulator, indicating the indispensability of electron correlation. Our work highlights the critical role of interlayer stacking order and reveals an important role of the Coulomb correlation effects in the electronic properties of the CCDW phase $1T$-NbS_2. Furthermore, we propose stacking-controllable metal-insulator transitions, metamagnetic transitions, and exotic quantum phase perhaps existing in the promising $1T$-NbS_2, which will draw intensive attention.

ACKNOWLEDGMENTS

We would like to thank Dr. Sung-Hoon Lee from Kyung Hee University for the fruitful discussion. The computational work in this research was carried out at Shanxi Supercomputing Center, and the calculations were performed on TianHe-2. The work was sponsored by the National Natural Science Foundation of China (Grant No. 11864008) and Guangxi Natural Science Foundation (Grants No. 2018AD19200 and No. 2019GXNSFGA245006). C.A. is supported by the Foundation for Polish Science through the International Research Agendas program cofinanced by the European Union within the Smart Growth Operational Programme.

[1] G. Fiori, F. Bonaccorso, G. Iannaccone, T. Palacios, D. Neumaier, A. Seabaugh, S. K. Banerjee, and L. Colombo, Electronics based on two-dimensional materials, Nat. Nanotechnol. **9**, 768 (2014).

[2] A. K. Geim and I. V. Grigorieva, Van der Waals heterostructures, Nature (London) **499**, 419 (2013).

[3] K. S. Novoselov, A. Mishchenko, A. Carvalho, and A. H. Castro Neto, 2D materials and van der Waals heterostructures, Science **353**, aac9439 (2016).

[4] S. Carr, D. Massatt, S. Fang, P. Cazeaux, M. Luskin, and E. Kaxiras, Twistronics: Manipulating the electronic properties of two-dimensional layered structures through their twist angle, Phys. Rev. B **95**, 075420 (2017).

[5] R. Ribeiro-Palau, C. Zhang, K. Watanabe, T. Taniguchi, J. Hone, and C. R. Dean, Twistable electronics with dynamically rotatable heterostructures, Science **361**, 690 (2018).

[6] Y. Cao, V. Fatemi, S. Fang, K. Watanabe, T. Taniguchi, E. Kaxiras, and P. Jarillo-Herrero, Unconventional

superconductivity in magic-angle graphene superlattices, Nature (London) **556**, 43 (2018).

[7] M. Yankowitz, S. Chen, H. Polshyn, Y. Zhang, K. Watanabe, T. Taniguchi, D. Graf, and C. R. Dean, Tuning superconductivity in twisted bilayer graphene, Science **363**, 1059 (2019).

[8] X. Lu, P. Stepanov, W. Yang, M. Xie, M. A. Aamir, I. Das, C. Urgell, K. Watanabe, T. Taniguchi, G. Zhang, A. Bachtold, A. H. MacDonald, and D. K. Efetov, Superconductors, orbital magnets and correlated states in magic-angle bilayer graphene, Nature (London) **574**, 653 (2019).

[9] Y. Cao, V. Fatemi, A. Demir, S. Fang, S. L. Tomarken, J. Y. Luo, J. D. Sanchez-Yamagishi, K. Watanabe, T. Taniguchi, E. Kaxiras, R. C. Ashoori, and P. Jarillo-Herrero, Correlated insulator behaviour at half-filling in magic-angle graphene superlattices, Nature (London) **556**, 80 (2018).

[10] A. L. Sharpe, E. J. Fox, A. W. Barnard, J. Finney, K. Watanabe, T. Taniguchi, M. A. Kastner, and D. Goldhaber-Gordon, Emergent ferromagnetism near three-quarters filling in twisted bilayer graphene, Science **365**, 605 (2019).

[11] M. Serlin, C. L. Tschirhart, H. Polshyn, Y. Zhang, J. Zhu, K. Watanabe, T. Taniguchi, L. Balents, and A. F. Young, Intrinsic quantized anomalous Hall effect in a moiré heterostructure, Science **367**, 900 (2020).

[12] L. Li and M. Wu, Binary compound bilayer and multilayer with vertical polarizations: Two-dimensional ferroelectrics, multiferroics, and nanogenerators, ACS Nano **11**, 6382 (2017).

[13] K. Yasuda, X. Wang, K. Watanabe, T. Taniguchi, and P. Jarillo-Herrero, Stacking-engineered ferroelectricity in bilayer boron nitride, Science **372**, 1458 (2021).

[14] P. Jiang, C. Wang, D. Chen, Z. Zhong, Z. Yuan, Z. Lu, and W. Ji, Stacking tunable interlayer magnetism in bilayer CrI_3, Phys. Rev. B **99**, 144401 (2019).

[15] W. Chen, Z. Sun, Z. Wang, L. Gu, X. Xu, S. Wu, and C. Gao, Direct observation of van der Waals stacking-dependent interlayer magnetism, Science **366**, 983 (2019).

[16] T. Ritschel, H. Berger, and J. Geck, Stacking-driven gap formation in layered $1T$-TaS_2, Phys. Rev. B **98**, 195134 (2018).

[17] T. Ritschel, J. Trinckauf, K. Koepernik, B. Büchner, M. v. Zimmermann, H. Berger, Y. I. Joe, P. Abbamonte, and J. Geck, Orbital textures and charge density waves in transition metal dichalcogenides, Nat. Phys. **11**, 328 (2015).

[18] C. J. Butler, M. Yoshida, T. Hanaguri, and Y. Iwasa, Mottness versus unit-cell doubling as the driver of the insulating state in $1T$-TaS_2, Nat. Commun. **11**, 2477 (2020).

[19] L. Ma, C. Ye, Y. Yu, X. Lu, X. Niu, S. Kim, D. Feng, D. Tománek, Y. Son, X. Chen, and Y. Zhang, A metallic mosaic phase and the origin of Mott-insulating state in $1T$-TaS_2, Nat. Commun. **7**, 10956 (2016).

[20] J. A. Wilson, F. J. Di Salvo, and S. Mahajan, Charge-density waves and superlattices in the metallic layered transition metal dichalcogenides, Adv. Phys. **24**, 117 (1975).

[21] P. Fazekas and E. Tosatti, Charge carrier localization in pure and doped $1T$-TaS_2, Physica B+C **99**, 183 (1980).

[22] S. H. Lee, J. S. Goh, and D. Cho, Origin of the Insulating Phase and First-Order Metal-Insulator Transition in $1T$-TaS_2, Phys. Rev. Lett. **122**, 106404 (2019).

[23] E. Martino, A. Pisoni, L. Ćirić, A. Arakcheeva, H. Berger, A. Akrap, C. Putzke, P. J. W. Moll, I. Batistić, E. Tutiš, L. Forró, and K. Semeniuk, Preferential out-of-plane conduction and quasi-one-dimensional electronic states in layered $1T$-TaS_2, npj 2D Mater. Appl. **4**, 7 (2020).

[24] X. L. Yu, D. Y. Liu, Y. M. Quan, J. Wu, H. Q. Lin, K. Chang, and L. J. Zou, Electronic correlation effects and orbital density wave in the layered compound $1T$-TaS_2, Phys. Rev. B **96**, 125138 (2017).

[25] Y. D. Wang, Y. D. Wang, W. L. Yao, Z. M. Xin, T. T. Han, Z. G. Wang, L. Chen, C. Cai, Yuan Li, and Y. Zhang, Band insulator to Mott insulator transition in $1T$-TaS_2, Nat. Commun. **11**, 4215 (2020).

[26] P. Darancet, A. J. Millis, and C. A. Marianetti, Three-dimensional metallic and two-dimensional insulating behavior in octahedral tantalum dichalcogenides, Phys. Rev. B **90**, 045134 (2014).

[27] G. von Witte, T. Kißlinger, J. G. Horstmann, K. Rossnagel, M. A. Schneider, C. Ropers, and L. Hammer, Surface structure and stacking of the commensurate (13×13)R13.9° charge density wave phase of $1T$-TaS_2 (0001), Phys. Rev. B **100**, 155407 (2019).

[28] R. Hovden, A. W. Tsen, P. Liu, B. H. Savitzky, I. E. Baggari, Y. Liu, W. Lu, Y. Sun, P. Kim, A. N. Pasupathy, and L. F. Kourkoutis, Atomic lattice disorder in charge-density-wave phases of exfoliated dichalcogenides ($1T$-TaS_2), Proc. Natl. Acad. Sci. USA **113**, 11420 (2016).

[29] Z. Wu, K. Bu, W. Zhang, Y. Fei, Y. Zheng, J. Gao, X. Luo, Z. Liu, Y.-P. Sun, and Y. Yin, Effect of stacking order on the electronic state of $1T$-TaS_2, Phys. Rev. B **105**, 035109 (2022).

[30] D. Cho, S. Cheon, K. S. Kim, S. H. Lee, Y. H. Cho, S. W. Cheong, and H. W. Yeom, Nanoscale manipulation of the Mott insulating state coupled to charge order in $1T$-TaS_2, Nat. Commun. **7**, 10453 (2016).

[31] W. Wang, B. Wang, Z. Gao, G. Tang, W. Lei, X. Zheng, H. Li, X. Ming, and C. Autieri, Charge density wave instability and pressure-induced superconductivity in bulk $1T$-NbS_2, Phys. Rev. B **102**, 155115 (2020).

[32] C. Tresca and M. Calandra, Charge density wave and spin 1/2 insulating state in single layer $1T$-NbS_2, 2D Mater. **6**, 035041 (2019).

[33] W. Wang, W. Lei, X. Zheng, H. Li, X. Tang, and X. Ming, Electronic structure and phase transition engineering in NbS_2: Crucial role of van der Waals interactions, Chin. Phys. B **29**, 056201 (2020).

[34] Z. E. Youbi, S. W. Jung, C. Richter, K. Hricovini, C. Cacho, and M. D. Watson, Fermiology and electron-phonon coupling in the $2H$ and $3R$ polytypes of NbS_2, Phys. Rev. B **103**, 155105 (2021).

[35] M. Leroux, L. Cario, A. Bosak, and P. Rodière, Traces of charge density waves in NbS_2, Phys. Rev. B **97**, 195140 (2018).

[36] I. Guillamón, H. Suderow, S. Vieira, L. Cario, P. Diener, and P. Rodière, Superconducting Density of States and Vortex Cores of $2H$-NbS_2, Phys. Rev. Lett. **101**, 166407 (2008).

[37] R. Bianco, I. Errea, L. Monacelli, M. Calandra, and F. Mauri, Quantum enhancement of charge density wave in NbS_2 in the two-dimensional limit, Nano Lett. **19**, 3098 (2019).

[38] E. Martino, C. Putzke, M. König, P. Moll, H. Berger, D. LeBoeuf, M. Leroux, C. Proust, A. Akrap, H. Kirmse, C. Koch, S. Zhang, Q. Wu, O. V. Yazyev, L. Forró, and K. Semeniuk,

Unidirectional Kondo scattering in layered NbS_2, npj 2D Mater. Appl. **5**, 86 (2021).

[39] K. T. Law and P. A. Lee, $1T$-TaS_2 as a quantum spin liquid, Proc. Natl. Acad. Sci. USA **114**, 6996 (2017).

[40] W. Y. He, X. Y. Xu, G. Chen, K. T. Law, and P. A. Lee, Spinon Fermi Surface in a Cluster Mott Insulator Model on a Triangular Lattice and Possible Application to $1T$-TaS_2, Phys. Rev. Lett. **121**, 046401 (2018).

[41] M. Klanjšek, A. Zorko, R. Žitko, J. Mravlje, Z. Jagličić, P. K. Biswas, P. Prelovšek, D. Mihailovic, and D. Arčon, A high-temperature quantum spin liquid with polaron spins, Nat. Phys. **13**, 1130 (2017).

[42] M. Kratochvilova, A. D. Hillier, A. R. Wildes, L. Wang, S. W. Cheong, and J. G. Park, The low-temperature highly correlated quantum phase in the charge-density-wave $1T$-TaS_2 compound, npj Quantum Mater. **2**, 42 (2017).

[43] A. Ribak, I. Silber, C. Baines, K. Chashka, Z. Salman, Y. Dagan, and A. Kanigel, Gapless excitations in the ground state of $1T$-TaS_2, Phys. Rev. B **96**, 195131 (2017).

[44] C.-K. Li, X.-P. Yao, and G. Chen, Fractionalization on the surface: Is type-II terminated $1T$-TaS_2 surface an anomalously realized spin liquid, arXiv:2109.08093.

[45] S. Mañas-Valero, B. M. Huddart, T. Lancaster, E. Coronado, and F. L. Pratt, Quantum phases and spin liquid properties of $1T$-TaS_2, npj Quantum Mater. **6**, 69 (2021).

[46] G. Kresse and J. Hafner, *Ab initio* molecular dynamics for liquid metals, Phys. Rev. B **47**, 558 (1993).

[47] G. Kresse and J. Furthmüller, Efficiency of ab-initio total energy calculations for metals and semiconductors using a plane-wave basis set, Comput. Mater. Sci. **6**, 15 (1996).

[48] J. P. Perdew, K. Burke, and M. Ernzerhof, Generalized Gradient Approximation Made Simple, Phys. Rev. Lett. **77**, 3865 (1996).

[49] G. Kresse and D. Joubert, From ultrasoft pseudopotentials to the projector augmented-wave method, Phys. Rev. B **59**, 1758 (1999).

[50] H. J. Monkhorst and J. D. Pack, Special points for Brillouin-zone integrations, Phys. Rev. B **13**, 5188 (1976).

[51] S. Grimme, J. Antony, S. Ehrlich, and H. Krieg, A consistent and accurate ab initio parametrization of density functional dispersion correction (DFT-D) for the 94 elements H-Pu, J. Chem. Phys. **132**, 154104 (2010).

[52] J. Klimeš, D. R. Bowler, and A. Michaelides, Chemical accuracy for the van der Waals density functional, J. Phys.: Condens. Matter **22**, 022201 (2009).

[53] K. Lee, É. D. Murray, L. Kong, B. I. Lundqvist, and D. C. Langreth, Higher-accuracy van der Waals density functional, Phys. Rev. B **82**, 081101(R) (2010).

[54] See Supplemental Material at http://link.aps.org/supplemental/10.1103/PhysRevB.105.035119 for a comparison of the calculated results by DFT-D3 and optB88-vdW methods, the nonmagnetic and antiferromagnetic band structure of the T_0 stacking configuration, the charge density maps of the T_2 and T_3 stacking orders, and nonmagnetic state band structure of the T_2, T_3, T_4, T_{02}, T_{03}, and T_{04} stacking configurations.

[55] N. Marom, J. Bernstein, J. Garel, A. Tkatchenko, E. Joselevich, L. Kronik, and O. Hod, Stacking and Registry Effects in Layered Materials: The Case of Hexagonal Boron Nitride, Phys. Rev. Lett. **105**, 046801 (2010).

[56] M. Naito, H. Nishihara, and S. Tanaka, Nuclear magnetic resonance and nuclear quadrupole resonance study of ^{181}Ta in the commensurate charge density wave state of $1T$-TaS_2, J. Phys. Soc. Jpn. **55**, 2410 (1986).

[57] A. Fuhrmann, D. Heilmann, and H. Monien, From Mott insulator to band insulator: A dynamical mean-field theory study, Phys. Rev. B **73**, 245118 (2006).

[58] S. S. Kancharla and S. Okamoto, Band insulator to Mott insulator transition in a bilayer Hubbard model, Phys. Rev. B **75**, 193103 (2007).

[59] M. Calandra, Phonon-Assisted Magnetic Mott-Insulating State in the Charge Density Wave Phase of Single-Layer 1T-$NbSe_2$, Phys. Rev. Lett. **121**, 026401 (2018).

[60] H. Watanabe, Hiroshi, T. Shirakawa, and S. Yunoki, Theoretical study of insulating mechanism in multiorbital Hubbard models with a large spin-orbit coupling: Slater versus Mott scenario in Sr_2IrO_4, Phys. Rev. B **89**, 165115 (2014).

[61] J. Yang, L. Hao, D. Meyers, T. Dasa, L. Xu, L. Horak, P. Shafer, E. Arenholz, G. Fabbris, Y. Choi, D. Haskel, J. Karapetrova, J. W. Kim, P. J. Ryan, H. Xu, C. D. Batista, M. P. M. Dean, and J. Liu, Strain-Modulated Slater-Mott Crossover of Pseudospin-Half Square-Lattice in $(SrIrO_3)_1/(SrTiO_3)_1$ Superlattices, Phys. Rev. Lett. **124**, 177601 (2020).

[62] D. J. Groenendijk, C. Autieri, J. Girovsky, M. C. Martinez-Velarte, N. Manca, G. Mattoni, A. M. R. V. L. Monteiro, N. Gauquelin, J. Verbeeck, A. F. Otte, M. Gabay, S. Picozzi, and A. D. Caviglia, Spin-Orbit Semimetal $SrIrO_3$ in the Two-Dimensional Limit, Phys. Rev. Lett. **119**, 256403 (2017).

[63] P. Lazar, J. Martincová, and M. Otyepka, Structure, dynamical stability, and electronic properties of phases in TaS_2 from a high-level quantum mechanical calculation, Phys. Rev. B **92**, 224104 (2015).

[64] D. Shin, N. Tancogne-Dejean, J. Zhang, M. S. Okyay, A. Rubio, and N. Park, Identification of the Mott Insulating Charge Density Wave State in $1T$-TaS_2, Phys. Rev. Lett. **126**, 196406 (2021).

[65] C. J. Carmalt, T. D. Manning, I. P. Parkin, E. S. Peters, and A. L. Hector, Formation of a new (1T) trigonal NbS_2 polytype via atmospheric pressure chemical vapour deposition, J. Mater. Chem. **14**, 290 (2004).